MAJOR ARTICLE

Evaluation of Monkeypox Disease Progression by Molecular Imaging

Julie Dyall,[1,a] Reed F. Johnson,[2,a] Dar-Yeong Chen,[1,b] Louis Huzella,[1] Dan R. Ragland,[1] Daniel J. Mollura,[1,3] Russell Byrum,[1] Richard C. Reba,[1,3] Gerald Jennings,[1] Peter B. Jahrling,[1,2] Joseph E. Blaney,[2] and Jason Paragas[1]

[1]Integrated Research Facility, National Institute of Allergy and Infectious Diseases, [2]Emerging Viral Pathogens Section, National Institute of Allergy and Infectious Diseases, and [3]Center for Infectious Disease Imaging, Radiology and Imaging Sciences, Clinical Center, National Institutes of Health, Bethesda, Maryland

Infection of nonhuman primates (NHPs) with monkeypox virus (MPXV) is currently being developed as an animal model of variola infection in humans. We used positron emission tomography and computed tomography (PET/CT) to identify inflammatory patterns as predictors for the outcome of MPXV disease in NHPs. Two NHPs were sublethally inoculated by the intravenous (IV) or intrabronchial (IB) routes and imaged sequentially using fluorine-18 fluorodeoxyglucose (^{18}FDG) uptake as a nonspecific marker of inflammation/immune activation. Inflammation was observed in the lungs of IB-infected NHPs, and bilobular involvement was associated with morbidity. Lymphadenopathy and immune activation in the axillary lymph nodes were evident in IV- and IB-infected NHPs. Interestingly, the surviving NHPs had significant ^{18}FDG uptake in the axillary lymph nodes at the time of MPXV challenge with no clinical signs of illness, suggesting an association between preexisting immune activation and survival. Molecular imaging identified patterns of inflammation/immune activation that may allow risk assessment of monkeypox disease.

Monkeypox virus (MPXV) is an emerging zoonotic pathogen that results in up to 10% mortality in humans [1]. Due to the similarity of orthopoxviruses, live vaccines used in smallpox eradication programs induced cross-protective immunity against MPXV infections. Successful eradication of smallpox rendered vaccinations unnecessary but has resulted in an increasingly unvaccinated population susceptible to MPXV infection. In addition, the increased efficiency of human-to-human transmission of MPXV, the bioterrorism threat of smallpox and MPXV, and the increase in the observed number of animal hosts position MPXV as a potential large-scale public health threat [2–4]. Knowledge of clinical manifestations and temporal progression of monkeypox disease is limited to data collected from rare outbreaks in remote regions of the Congo Basin and West Africa. However, a recent monkeypox outbreak in the United States led to a more complete clinical characterization with detailed analysis of the risk factors of MPXV transmission [5–7]. To date, clinical observations show that monkeypox infection resembles variola infection, with fever and malaise followed by a peripherally distributed vesiculopustular rash [8–10]. However, pronounced lymphadenopathy develops in the majority of MPXV patients, distinguishing it from variola virus infection [11]. To gain better understanding of monkeypox disease and counteract the threat of human orthopoxvirus infection, animal models using nonhuman primates (NHPs) are being developed using different routes of MPXV infection. Intravenous (IV) inoculation of MPXV in NHPs results in an accelerated (shortened prodromal phase) fulminant disease course with severe lesions. Intratracheal, intranasal, and intrabronchial (IB) administration of MPXV mimics more closely the aerosol transmission route of MPXV in humans and better reflects the temporal progression of human disease [12–14].

Received 24 May 2011; accepted 9 August 2011.

[a]Authors contributed equally.

[b]Present affiliation: Synarc Inc, San Francisco, California

Presented in part: XVIII International Poxvirus, Asfivirus, and Iridovirus Symposium, Sedona, Arizona, 5–10 June 2010. Abstract P6.28.

Correspondence: Peter B. Jahrling, PhD, Integrated Research Facility, National Institute of Allergy and Infectious Diseases, National Institutes of Health, 8200 Research Plaza, Frederick, MD 21702 (jahrlingp@niaid.nih.gov).

The Journal of Infectious Diseases 2011;204:1902–11
Published by Oxford University Press on behalf of the Infectious Diseases Society of America 2011.
0022-1899 (print)/1537-6613 (online)/2011/20412-0013$14.00
DOI: 10.1093/infdis/jir663

With the limited capability to study MPXV and smallpox disease in humans, it is increasingly clear that a more thorough characterization of disease progression in poxvirus animal models is required. Nuclear imaging modalities, such as positron emission tomography (PET) and single photon emission computed tomography (SPECT), offer the opportunity to study viral and host processes at the cellular and molecular levels in intact organisms. PET, which uses fluorine-18 fluorodeoxyglucose (^{18}FDG) as a biomarker to detect elevated glucose metabolism in activated cells, is the most commonly used and validated molecular imaging technique in the clinic. ^{18}FDG-PET imaging allows rapid detection and localization of neoplasms and foci of inflammation with high sensitivity. ^{18}FDG-PET imaging in the clinic, in combination with anatomical imaging modalities such as computed tomography (CT) with high-spatial resolution, has proven to be invaluable for the diagnosis and staging of cancer as well as rapid detection and localization of foci of infection and/or inflammation [15].

Nuclear imaging modalities have rarely been used to investigate viral infections in NHPs. One reason for this lies in limited access to this costly imaging equipment for animal studies on human pathogens that require high containment. Two recent reports describe ^{18}FDG-PET/CT imaging in NHP models for AIDS to study activation patterns of lymphoid tissues during disease [16, 17]. Interestingly, the findings revealed a correlation between the pattern of activation of lymph nodes (LNs) and different stages of the disease. A subsequent small study in patients with human immunodeficiency virus (HIV) showed a distinctive pattern of lymphoid tissue activation, indicating that LNs in different areas of the body have specialized roles to play during the course of disease [18].

The following study investigates the use of ^{18}FDG-PET/CT imaging to visualize in vivo patterns of metabolic activity during MPXV infection in NHPs. The present study was initiated to (1) determine if PET/CT imaging could be used to nondestructively monitor or stage disease severity in real time, (2) identify patterns of immune activation/inflammation associated with disease outcome, and (3) differentiate route of inoculation in the development of inflammation.

METHODS

Virus

MPXV Zaire 79 strain (V-79-I-005) was propagated in Vero E6 cells at a multiplicity of infection (MOI) of 0.1 for 7 days. Inoculum for challenge experiments was prepared by disruption of Vero E6 cells in an Ultrasonic Processor VCX-750 (Sonics & Materials) for 120 seconds at 40% power on ice, followed by centrifugation (500*g* for 10 minutes at 4°C).

Inoculation of NHPs

Cynomolgus macaques of both sexes, ranging from 3 to 4 kg, were housed in biosafety level 3 containment. Prior to enrollment, NHPs were screened to be negative for simian retrovirus, simian T-cell leukemia, vaccinia virus (VACV), cowpox virus (CPXV), and MPXV, and had no detectable antibodies against VACV as determined by flow cytometry against VACV containing the green fluorescent protein [19]. Inoculations were performed as described by Johnson and Dyall [20]. IV inoculation was performed by injecting 1 mL of virus inoculum into the left saphenous vein, and IB inoculation was performed by administering 1 mL of virus inoculum into the left tertiary bronchus using a pediatric bronchoscope. All animal experiments were approved by the National Institute of Allergy and Infectious Diseases Animal Care and Use Committee and adhered to National Institutes of Health policies.

PET/CT Imaging

^{18}FDG-PET images were acquired using a Focus-220 (Siemens AG) with 0.90-mm pixel resolution and 0.8-mm slice thickness for 96 slices per bed location. Two bed locations were scanned to cover the NHP from neck down to pelvis. NHPs were anesthetized with telazol and received IV injections of 1–5 mCi ^{18}FDG. After 1 hour, the PET scans were performed on the NHPs following intubation and anesthesia with isoflurane (1.5%). CT images were acquired using CereTom (NeuroLogica) with 120 kV (peak), 5 mA, 1.25-mm scan thickness for 190 slices with 0.49 × 0.49 mm in-plane resolution. The contrast agent Isovue 300 (Bracco Diagnostics) was administered IV at 3 mL/kg animal weight, followed by 10 mL of saline flush administered by hand at approximately 1 mL/second. CT scans were conducted at 40 seconds and at 3 minutes after the injection of Isovue 300. Prior to the PET scan data acquisition, a transmission scan using Co-57 point source was conducted using the Focus 220 for the purpose of attenuation correction of the PET images. CT scans were conducted either immediately before or after PET imaging so that the animal positioning was not changed and the PET and CT scans could be fused for data analysis.

PET/CT Data Analysis

Fusion and analysis of PET and CT images was conducted using PMOD software (PMOD Technologies). Standard uptake value (SUV) calculation was performed using PMOD's algorithm with 6 cm × 6 cm × 6 cm Gaussian filtering. Volumes of interest (VOIs) for LNs were first drawn by manual contouring to outline each LN, followed with auto-isocontouring using 50% of the maximum value within the manual drawn VOI. Peak SUV (SUV_{max}) of each LN VOI was then calculated as the average of the 5 highest pixel counts. Each VOI for a lung site was first drawn with a boundary object volume that contained the lung field, followed with auto-isocontouring using 90% of the maximum value within the object volume. Peak SUV (SUV_{max}) of each lung VOI was then calculated as the average of the 5 highest pixel counts.

Virus Quantification by Real-Time Polymerase Chain Reaction

Viral load in whole blood was determined by quantitative polymerase chain reaction, as described previously [20, 21], using the

primer/probe 5'-GATGATGCAACTCTATCATGTA-3') directed at the HA (J7R) gene of MPXV. The limit of detection was 10 gene copies/mL.

Necropsy

Complete necropsies were performed at time of moribundity after animals were humanely euthanized by established guidelines. Animals that became clinically ill and subsequently recovered were euthanized and necropsied at day 36 after exposure. Tissue samples were collected from all major organs for histopathological analysis and determination of viral load.

Histology and Immunohistochemistry

Tissues were immersion-fixed in 10% phosphate-buffered formalin. Paraffin-embedded samples were processed into 4-μm sections by a microtome. Fixed slides were then stained with hematoxylin and eosin, rinsed, and coverslipped for examination via light microscopy. Immunohistochemical assays were performed on a Bond Polymer Refine Detection System. Positive controls included formalin-fixed, paraffin-embedded spleen, lymphoid tissue, or skin from NHPs infected with MPXV. Negative controls included spleen or lymphoid tissue from uninfected NHPs. Select tissues were evaluated for the presence of fibrin via the phosphotungstic-acid hematoxylin (PTAH) method.

RESULTS

Clinical Disease

Groups of 2 cynomolgus macaques were challenged by IV or IB inoculation with 5×10^6 or 5×10^5 plaque-forming units of MPXV, respectively, and were evaluated by standard virological methods and serial PET/CT imaging of the thoracic region (Table 1). Subuniformly lethal doses were used to elicit contrasting changes in biomarkers that might be predictors of morbidity. Importantly, the development of clinical signs, viremia, and neutralizing antibody activity in the infected NHPs was not affected by the imaging procedures and extended periods of anesthesia (Table 2). Mean days of fever onset and mean peak temperatures were within the range that we observed for nonimaged animals in a previous study, although statistical power is lacking due to small numbers of primates [20]. Lesions first appeared and lesion numbers peaked in similar fashion as for nonimaged animals, indicating that the kinetics of virus dissemination was not altered by imaging procedure for either route of infection. Time of death for the imaged IV-infected NHPs occurred on day 12 and for the imaged IB-infected NHPs on day 17. Both time points are within the historical range (days 9–18) for moribundity for the MPXV infection model in NHPs by either routes, demonstrating that imaging did not exacerbate progression of disease [22–24]. Magnitude and timing of the cytokine, peripheral blood mononuclear cell, and antibody responses were consistent with those in the nonimaged NHPs, demonstrating that imaging procedure did not interfere with strength of immune response to MPXV infection (data not shown).

PET/CT Imaging Demonstrated Severe Consolidation of the Lung in IB-Inoculated NHPs

One NHP from each group (IV-2 and IB-1) became severely ill and met euthanasia criteria prior to the end of the study (Table 1). Despite the previously reported lung involvement after IV infection, longitudinal PET/CT imaging demonstrated no consolidation or inflammation in the lung of NHPs infected by the IV route [20]. In contrast, CT imaging revealed severe consolidation for both IB-inoculated NHPs (Figure 1). On day 10 for IB-1, which succumbed to disease, areas of hazy attenuation mixed with patchy consolidation developed bilaterally and colocalized with ^{18}FDG uptake (Figure 1*A*). By day 17, when IB-1 became moribund, consolidation encompassed both the right and left lungs with the most severe inflammation observed (SUV_{max} = 19.4 and 19.3, respectively). Gross pathology and histology at necropsy confirmed the severe pneumonia observed by PET/CT imaging (Figure 1*B*). There were areas of pulmonary consolidation with areas of necrosis, abundant in fibrin (confirmed by PTAH staining; data not shown), mixed inflammation, edema, and some fibrosis consistent with radiological findings on day 17 (Figure 1*B*). An infiltrate consisting of neutrophils and

Table 1. Experimental Design of PET/CT Imaging

				Postinoculation scan on day:[b]				
NHP	Dose	Route	Preinoculation scan day[a]	1	2	3	4	5
IB-1	5×10^5	IB	−4	4	10	17[c]		
IB-2	5×10^5	IB	−8	2	8	13	23	34
IV-1	5×10^6	IV	−4	4	17	34		
IV-2	5×10^6	IV	−8	2	8 (12)[c]			

Abbreviations: IB, intrabronchial; IV, intravenous; NHP, nonhuman primate; PET/CT, positron emission tomography/computed tomography.

[a] Two animals were inoculated IB or IV on day 0. A preinfection PET/CT scan was performed on day –4 or –8 prior to infection to obtain baseline images of uninfected animals.

[b] After inoculation, up to 5 scans were performed on indicated days until day 34 after infection or until the NHP became moribund.

[c] IB-1 was imaged on day of endpoint (day 17), but IV-2 was not imaged on day of endpoint (day 12).

Table 2. Disease Progression for Imaged and Nonimaged Nonhuman Primates

	Intravenous (5×10^6 PFU)		Intrabronchial (5×10^5 PFU)	
	Imaged (n = 2)	Nonimaged (n = 6)[a]	Imaged (n = 2)	Nonimaged (n = 6)[a]
Mean day of fever onset	3.5	3.0	6.0	7.0
Temperature range[b]	102.8–103.5	102.0–103.6	102.5–102.6	102.1–104.3
Mean day of lesion appearance	6.0	5.3	9.0	9.1
Lesion range[c]	538–1215	134–661	182–235	13–615
Mean day of peak viremia	9.0	9.3	11.5	10.0
Mean peak viremia[d]	6.9	6.4	5.3	7.6
Day of death	12.0[e]	15.0[e]	17.0[e]	9.0[e]

Abbreviation: PFU, plaque-forming unit.

[a] Historical data from Johnson et al [20].

[b] Range of mean peak temperature (°F).

[c] Range of peak lesion numbers.

[d] Log_{10} gene copies/mL.

[e] Only 1 animal met endpoint criteria.

monocytes underscored areas of severe inflammation, and immunohistochemistry showed that these areas of consolidation were positive for MPXV antigen (Figure 1*B*).

Conversely, PET/CT imaging revealed that NHP IB-2 developed a severe pneumonia that almost completely resolved by day 34 (Figure 1*C*). PET/CT imaging allowed tracking of progression and regression of the lung disease. Consolidation correlating with a high level of inflammation in the right lung was first detected by PET/CT ($SUV_{max} = 22.2$) on day 8 but failed to disseminate to the left lobes, as was observed in the lethal infection of IB-1, suggesting that the dissemination of inflammation and consolidation to both lungs may correlate with disease outcome for the IB inoculation route. Inflammation in the lung was decreasing by day 23 and was reduced to a few foci with high ^{18}FDG uptake ($SUV_{max} = 14.2$) on day 34, while CT imaging revealed residual patches of hazy attenuation at this point. Histopathological examination on day 35 confirmed that lung consolidation had mostly resolved (data not shown).

PET/CT Imaging Tracks Lymphadenopathy in IB- and IV-Infected NHPs

Despite the difference in inoculation route, longitudinal PET/CT imaging demonstrated severe lymphadenopathy in nonsurviving NHPs with axillary LN size increasing 2-fold from baseline by day 8 and day 10 for IV-2 and IB-1, respectively (Figure 2*A* and *C*). Semiquantitative analysis of PET images indicated that the LNs also became increasingly metabolically active in addition to the physical increase in size indicating LN activation. ^{18}FDG uptake in axillary LNs for NHP IV-2 increased approximately 5-fold from preinfection levels ($SUV_{max} = 1.2–1.7$ to 10.9–13.7) on day 2 after inoculation. Histopathological examination on the axillary LNs from NHP IV-2, which succumbed on day 12, showed necrosis with lymphoid depletion and areas of intense staining for MPXV antigen, suggesting active viral replication (Figure 2*B*). Similarly, ^{18}FDG uptake in the axillary LNs of NHP IB-1 increased approximately 8-fold from day –4 to day 4 after infection prior to decreasing to an approximate 4-fold increase in activation state by day 17 (Figure 2*C*). While LN activation occurred as early as day 2, enlargement of the axillary LNs was not detected until day 8 in NHP IV-2. Similar kinetics was found for NHP IB-1, indicating that LN activation precedes lymphadenopathy by several days in the early phase of disease. This finding demonstrates how PET/CT imaging can simultaneously distinguish and compare kinetics of LN activation versus lymphadenopathy and thereby provides valuable information that could not have been acquired through standard techniques of pathogenesis studies. Histopathological examination of the axillary LNs revealed moderate lymphoid hyperplasia with few areas of necrosis containing few MPXV-antigen positive macrophages (Figure 2*D*). While indistinguishable by PET/CT imaging, the difference in LN histopathology at time of clinical endpoint between IV-2 and IB-1 may be indicative of the different stages of disease. Nevertheless, PET/CT imaging clearly detected the onset and magnitude of LN activation and lymphadenopathy in these lethal infections and revealed that they occur sequentially.

The surviving NHPs, IB-2 and IV-1, also had pronounced lymphadenopathy (Figures 3 and 4). Similar to the moribund NHPs, the size of the axillary LNs of the 2 survivors increased 2-fold from baseline by day 13 and day 17 for IB-2 and IV-1, respectively. However, there still was substantial ^{18}FDG uptake when IB-2 was convalescing and the lung consolidation had regressed. Histopathological examination of LNs on days 34 and 35, respectively, revealed continued LN activation and normal LN architecture with active germinal centers (Figures 3*B* and 4*B*). The findings in surviving NHPs contrast with the severe depletion and necrosis seen in LNs of the 2 moribund NHPs. The convalescent NHPs had no detectable viremia on day 35 (data not shown). However, the axillary LNs of both animals

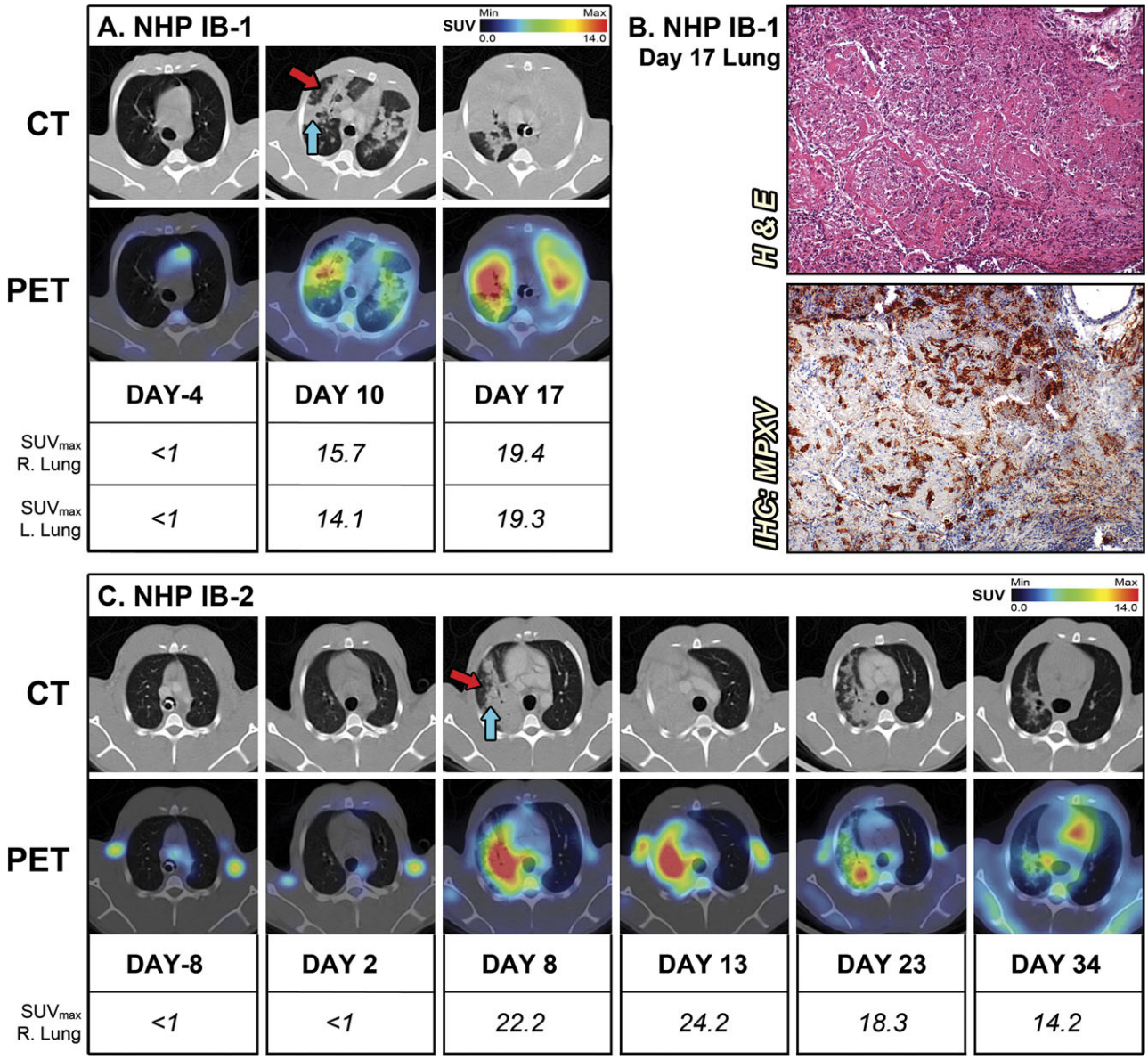

Figure 1. PET/CT) imaging of lung inflammation. *A,* For the nonhuman primate (NHP) IB-1 that succumbed to infection, sequential axial lung sections were imaged on day –4 and days 10 and 17 after infection. *B,* Histopathology and monkeypox virus (MPXV) antigen reactivity of lung on day 17. *C,* Sequential axial lung sections were imaged in surviving NHP IB-2 on day –8 and days 2, 8, 13, 23, and 34 after infection. (Red arrow) Hazy attenuation. (Blue arrow) Consolidated area. Maximum standard uptake values (SUV_{max}) for fluorine-18 fluorodeoxyglucose (^{18}F-FDG) in right and left sections of lung were determined on scanning days by PET. The PET/CT slice that was chosen for each image corresponds to the maximum SUV value determined in the volume of interest (VOI) of the lung. Abbreviations: H & E, hematoxylin and eosin; IB, intrabronchial; IHC, immunohistochemistry.

still contained a few MPXV-positive cells (Figures 3*B* and 4*B*). These likely represent isolated macrophages that pick up virus while circulating in the body during recovery from infection.

In contrast to the NHPs that succumbed, a retrospective analysis of the axillary LNs of IB-2 and IV-1 revealed a strikingly high degree of LN activation at the preinfection time points as measured by ^{18}FDG uptake in absence of lymphadenopathy (Figure 3*A*, IB-2: day –8, SUV_{max} of 10.1–11.4; and Figure 4*A*, IV-1: day –4, SUV_{max} of 14.5–19.7). This finding was surprising, since both animals appeared healthy during prestudy examination with no signs of disease or active infection. All NHPs had been thoroughly screened prior to study initiation and had no seroconversion against simian retrovirus, simian T-cell leukemia, and poxviruses. In addition, complete blood count data and circulating cytokine levels were assayed and did not suggest an infection, inflammatory state, or any differences between the survivors and nonsurvivors (data not shown). However, subtle changes in cell activation may have occurred and could have been missed at the time points tested.

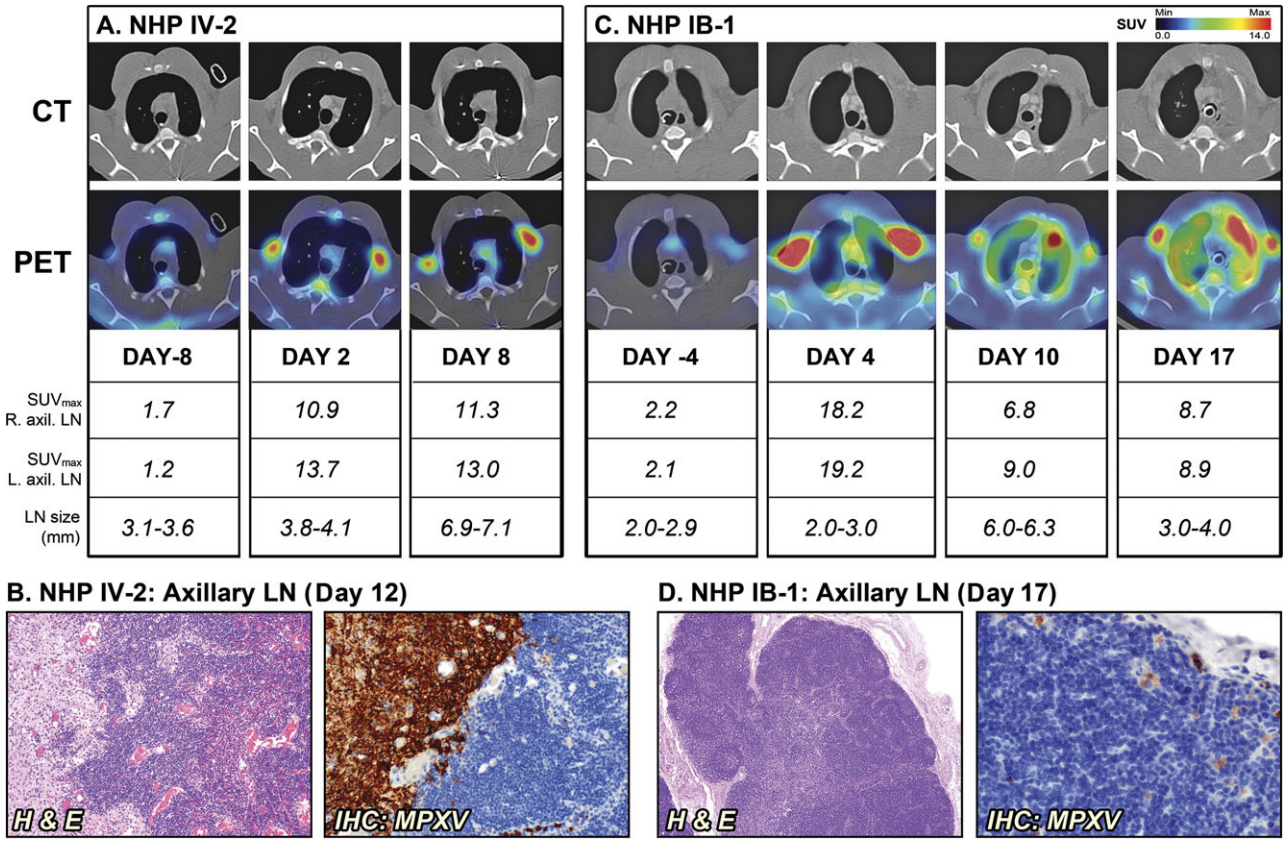

Figure 2. Sequential positron emission tomography/computed tomography (PET/CT) imaging of axillary lymph nodes (LNs) in nonhuman primates (NHPs) that succumbed to disease. *A,* NHP IV-2 was scanned on day –8 and days 2 and 8 after infection (d12, day of death). *B,* Histopathology of NHP IV-2 on day 12. *C,* NHP IB-1 was scanned on days –4 and days 10 and 17 after infection (day 17, day of death). *D,* Histopathology of NHP IB-1 on day 17. Fluorine-18 fluorodeoxyglucose (^{18}F-FDG) maximum standard uptake values (SUV_{max}) and short axis measurements of axillary LNs (LN size) were determined on scan days by PET and CT imaging, respectively. The PET/CT slice that was chosen corresponds to the maximum SUV value of the LNs. Abbreviations: H & E, hematoxylin and eosin; IB, intrabronchial; IHC, immunohistochemistry; IV, intravenous; MPXV, monkeypox virus.

DISCUSSION

This initial report on longitudinal ^{18}FDG-PET/CT imaging of MPXV infection in NHPs demonstrates the potential of molecular imaging to reveal disease phenomena that cannot be readily observed by other means. PET and CT imaging monitored progression and regression of disease in real time in NHPs infected with MPXV by 2 different routes of infection. The most significant difference related to route of infection was observed in images of the lung. Spread of severe inflammation in lungs was observed for both IB-inoculated NHPs, which was indicative of bronchopneumonia and has been reported to be a common complication of human smallpox [25, 26]. Although pneumonia has been found in IV-inoculated NHPs, this did not result in a detectable signal in the CT or PET images [20]. These imaging findings further support the value of the IB-infection model for studying the pathogenesis of orthopoxviruses.

Imaging revealed patterns of inflammation in lung and of immune activation in LNs associated with disease severity in this limited experiment of only 4 animals. One pattern of inflammation associated with disease severity was the correlation of disseminated lung consolidation and inflammation with lethality after IB inoculation. CT imaging of lungs in both IB-infected NHPs revealed characteristic patterns analogous to clinical findings of patients with infectious pneumonia and acute respiratory distress syndrome (ARDS) [27–29]. Areas of hazy attenuation (“ground-glass opacities”) are thought to be associated with an inflammatory process involving interstitial thickening and partial filling of the alveolar space with inflammatory cells, cellular debris, or edema. In the areas of dense consolidation, the alveolar air is thought to be completely, or almost completely, replaced by fluid, cells, or tissue [27, 28]. The NHP IB-1 that succumbed showed bilateral consolidation patterns with high ^{18}FDG uptake similar to findings observed for patients with ARDS [29]. At peak stage of lung involvement, some consolidated areas had no or low ^{18}FDG signal, indicating absence or necrosis of inflammatory cells. The lung of the surviving NHP IB-2 revealed similar PET/CT patterns; however, only 1 lung was affected, and over time consolidation was almost completely resolved as the animal recovered. These findings

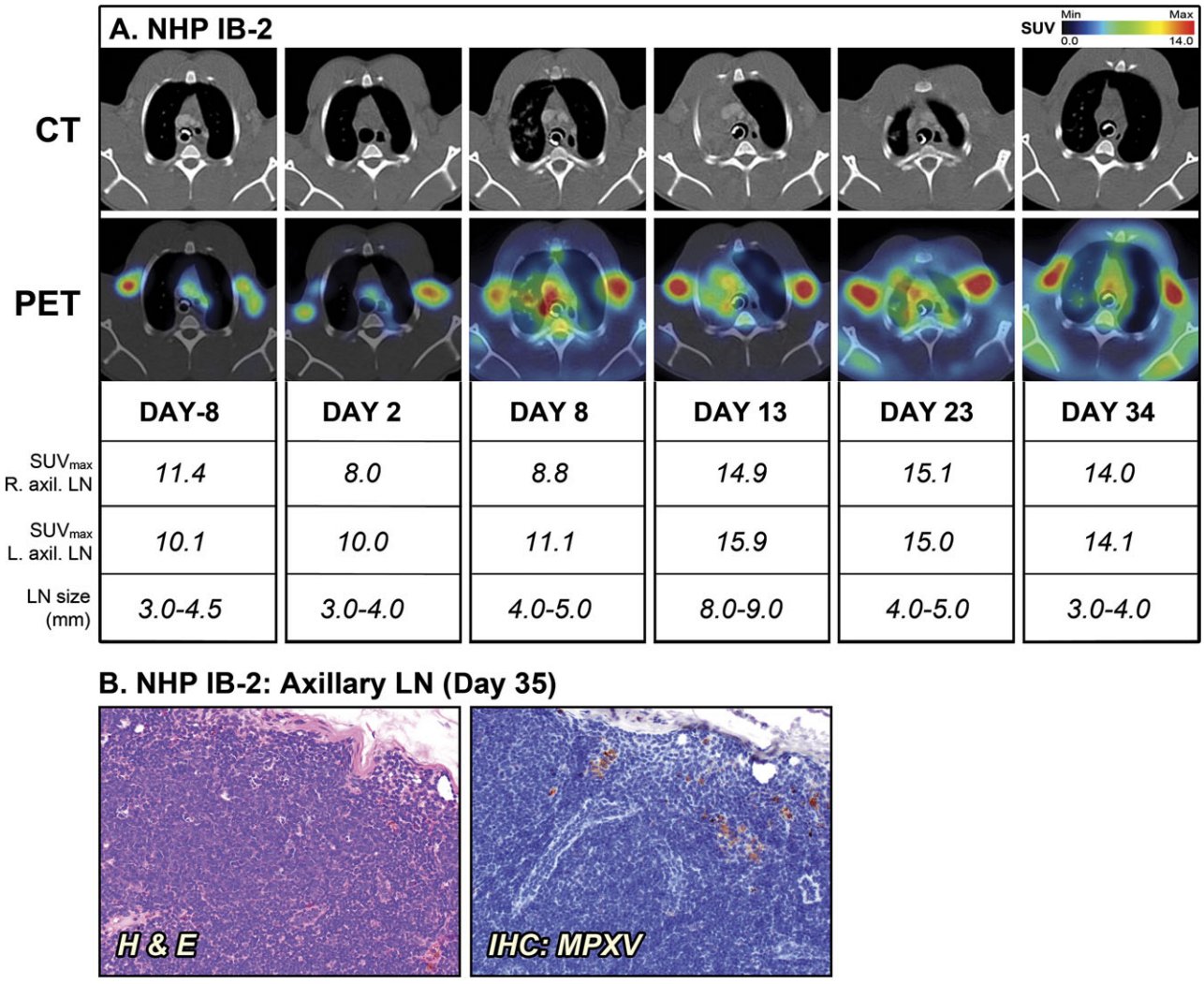

Figure 3. Positron emission tomography/computed tomography (PET/CT) imaging of axillary lymph nodes (LNs) in the surviving nonhuman primate (NHP) IB-2. *A,* Fluorine-18 fluorodeoxyglucose (^{18}FDG)–PET/CT scans were performed on days –8, 2, 8, 13, 23, and 34 of the study. Maximum standard uptake values (SUV_{max}) for ^{18}F-FDG uptake and short axis measurements of axillary LNs (LN size) were determined on scan days by PET and CT imaging, respectively. *B,* Histopathology and monkeypox virus (MPXV) antigen reactivity of axillary LN on day 35. The PET/CT slice that was chosen for each image corresponds to the maximum SUV value determined in the volume of interest (VOI) of the LNs. Abbreviations: H & E, hematoxylin and eosin; IB, intrabronchial; IHC, immunohistochemistry.

suggest that monitoring of the extent of lung inflammation may be an effective means of assessing disease severity after respiratory exposure.

MPXV infection in NHPs was associated with lymphadenopathy and an increase in ^{18}FDG uptake in axillary LNs. CT imaging demonstrated clear manifestation of lymphadenopathy for both routes of MPXV infection in all 4 animals. Metabolic activity in the axillary LNs was detected in PET images, and SUV_{max} data allowed semiquantitative analysis of the ^{18}FDG uptake over time. It is possible that the increase in metabolism is due to cell proliferation as part of a normal immune response, inflammation from cytocidal effects of MPXV, or cytotoxicity associated with the infiltration of activated immune cells. Further study will be required to discern the causes of the LN activation. After the destructive phase of the infection has passed, the LN remains enlarged as a result of the reorganization within the LNs to initiate immune response with strong B-cell and T-cell proliferation. This is exemplified in the current study by comparing the NHPs IV-2, which succumbed on day 12, and IV-1, which survived to study end. Both NHPs demonstrated lymphadenopathy and increased LN metabolism as measured by SUV during the study. But at necropsy of the moribund NHP, the LN was disrupted along with lymphocytolysis and hemorrhage, while the survivor's LN demonstrated a restored architecture with active germinal centers (Figures 2–4).

Interestingly, the 2 survivors (IB-2 and IV-1; Figures 3 and 4) presented high ^{18}FDG uptake in the axillary LNs before they were infected with MPXV, with no evidence of indications of infection or inflammation. The etiology of the intense ^{18}FDG signal is unclear, but it is possible that these 2 NHPs had unknown

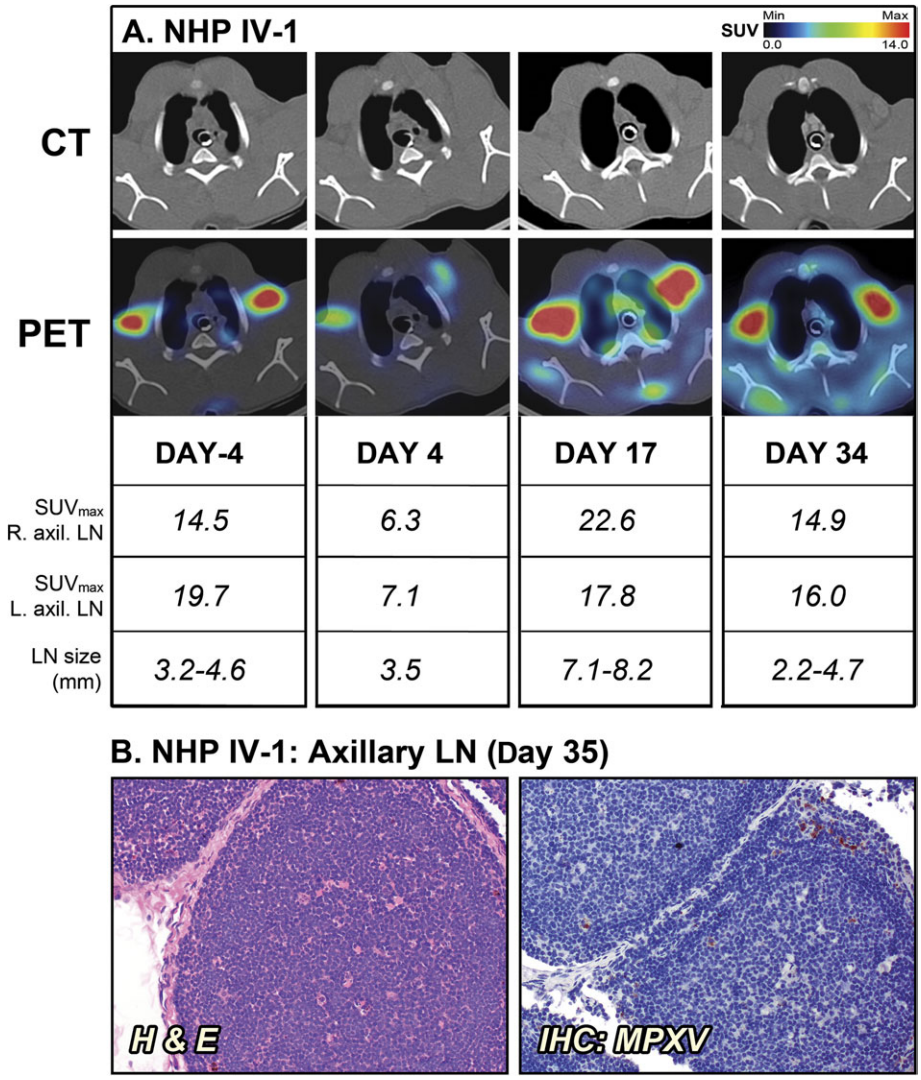

Figure 4. Positron emission tomography/computed tomography (PET/CT) imaging of axillary lymph nodes (LNs) in the surviving nonhuman primate (NHP) IV-1. *A,* Fluorine-18 fluorodeoxyglucose (^{18}FDG)–PET/CT scans were performed on days –4, 4, 17, and 34 of the study. Maximum standard uptake values (SUV_{max}) for ^{18}F-FDG uptake and short axis measurements of axillary LNs (LN size) were determined on scan days by PET and CT imaging, respectively. *B,* Histopathology and monkeypox virus (MPXV) antigen reactivity of axillary LN on day 35. The PET/CT slice that was chosen for each image corresponds to the maximum SUV value determined in the volume of interest (VOI) of the LNs. Abbreviations: H & E, hematoxylin and eosin; IHC, immunohistochemistry; IV, intravenous.

subclinical infections or were recovering from an unknown infection and that the increased metabolism corresponded to the long-term immune response to this earlier infection. Protection from a second infection by activated innate or adaptive immunity directed against a previous pathogen encounter has been reported [30–34]. The significance of our finding will be pursued in future studies with a greater number of animals.

The characterization of LNs, as described here, in response to acute infection is an increasingly important feature of diagnostic imaging. A key imaging finding in the diagnosis of acute anthrax is hemorrhagic lymphadenopathy in which mediastinal widening on chest radiography with enlarged LNs on CT was found to be helpful in early diagnosis [35, 36]. On the contrary, the absence of lymphadenopathy on CT for cases of swine-origin H1N1 and avian-origin H5N1 influenzas was a striking feature given the severe pulmonary complications associated with these infections [37–40]. Therefore, the monitoring of nodal disease is an important component of infectious disease and immunologic investigations. In the clinic, PET and CT imaging are being evaluated as tools for diagnosis and management of patients with infections such as inhalational anthrax, tuberculosis, severe acute respiratory syndrome, and H1N1 swine flu as well as fever of unknown origin [41–46]. Timely diagnosis is crucial for initiating rapid treatment and lowering mortality rate of infections, and PET/CT scans for patients with an infectious disease have shown the potential to help with follow-up diagnostic measures and reduce unnecessary invasive procedures, morbidity, and cost [42–44].

Our findings demonstrate the potential of PET imaging in pathogenesis studies for providing valuable serial data on metabolic activity and disease progression in the same subject. Further development of molecular imaging of MPXV and other high-consequence viral agents will improve methodology to study the progression and resolution of viral pathogenesis in individual subjects and identify efficacious countermeasures that modify disease progression. The continued identification of distinctive patterns in PET/CT images, using biomarkers of inflammation or infection, will contribute to developing predictive algorithms for early diagnosis and evaluation of infections.

Notes

Acknowledgments. The authors thank Jennifer Hufton, Christopher Leyson, Catherine Jett, Cindy Allan, Rebecca Kurnat, Erika Zommer, Isis Alexander, Nick Oberlander, and Bernardo Rosa for their contribution to these studies.

Financial support. This work was supported by the Division of Intramural Research of the National Institute of Allergy and Infectious Diseases (NIAID); Integrated Research Facility (NIAID, Division of Clinical Research); and Battelle Memorial Institute's prime contract with NIAID (HHSN272200200016I).

Potential conflicts of interest. All authors: No reported conflicts.

All authors have submitted the ICMJE Form for Disclosure of Potential Conflicts of Interest. Conflicts that the editors consider relevant to the content of the manuscript have been disclosed.

References

1. Likos AM, Sammons SA, Olson VA, et al. A tale of two clades: monkeypox viruses. J Gen Virol **2005**; 86:2661–72.
2. Heymann DL, Szczeniowski M, Esteves K. Re-emergence of monkeypox in Africa: a review of the past six years. Br Med Bull **1998**; 54:693–702.
3. Learned LA, Reynolds MG, Wassa DW, et al. Extended interhuman transmission of monkeypox in a hospital community in the Republic of the Congo, 2003. Am J Trop Med Hyg **2005**; 73:428–34.
4. Parker S, Nuara A, Buller RM, Schultz DA. Human monkeypox: an emerging zoonotic disease. Future Microbiol **2007**; 2:17–34.
5. Huhn GD, Bauer AM, Yorita K, et al. Clinical characteristics of human monkeypox, and risk factors for severe disease. Clin Infect Dis **2005**; 41:1742–51.
6. Reynolds MG, Davidson WB, Curns AT, et al. Spectrum of infection and risk factors for human monkeypox, United States, 2003. Emerg Infect Dis **2007**; 13:1332–9.
7. Reynolds MG, Yorita KL, Kuehnert MJ, et al. Clinical manifestations of human monkeypox influenced by route of infection. J Infect Dis **2006**; 194:773–80.
8. Arita I, Jezek Z, Khodakevich L, Ruti K. Human monkeypox: a newly emerged orthopoxvirus zoonosis in the tropical rain forests of Africa. Am J Trop Med Hyg **1985**; 34:781–9.
9. Jezek Z, Grab B, Dixon H. Stochastic model for interhuman spread of monkeypox. Am J Epidemiol **1987**; 126:1082–92.
10. Nalca A, Rimoin AW, Bavari S, Whitehouse CA. Reemergence of monkeypox: prevalence, diagnostics, and countermeasures. Clin Infect Dis **2005**; 41:1765–71.
11. Lederman ER, Reynolds MG, Karem K, et al. Prevalence of antibodies against orthopoxviruses among residents of Likouala region, Republic of Congo: evidence for monkeypox virus exposure. Am J Trop Med Hyg **2007**; 77:1150–6.
12. Saijo M, Ami Y, Suzaki Y, et al. Virulence and pathophysiology of the Congo Basin and West African strains of monkeypox virus in non-human primates. J Gen Virol **2009**; 90:2266–71.
13. Zaucha GM, Jahrling PB, Geisbert TW, Swearengen JR, Hensley L. The pathology of experimental aerosolized monkeypox virus infection in cynomolgus monkeys (*Macaca fascicularis*). Lab Invest **2001**; 81:1581–600.
14. Stittelaar KJ, van Amerongen G, Kondova I, et al. Modified vaccinia virus Ankara protects macaques against respiratory challenge with monkeypox virus. J Virol **2005**; 79:7845–51.
15. Curran SD, Muellner AU, Schwartz LH. Imaging response assessment in oncology. Cancer Imaging **2006**; 6:S126–30.
16. Scharko AM, Perlman SB, Hinds PW 2nd, Hanson JM, Uno H, Pauza CD. Whole body positron emission tomography imaging of simian immunodeficiency virus-infected rhesus macaques. Proc Natl Acad Sci U S A **1996**; 93:6425–30.
17. Wallace M, Pyzalski R, Horejsh D, et al. Whole body positron emission tomography imaging of activated lymphoid tissues during acute simian-human immunodeficiency virus 89.6PD infection in rhesus macaques. Virology **2000**; 274:255–61.
18. Scharko AM, Perlman SB, Pyzalski RW, Graziano FM, Sosman J, Pauza CD. Whole-body positron emission tomography in patients with HIV-1 infection. Lancet **2003**; 362:959–61.
19. Earl PL, Americo JL, Moss B. Development and use of a vaccinia virus neutralization assay based on flow cytometric detection of green fluorescent protein. J Virol **2003**; 77:10684–8.
20. Johnson RF, Dyall J, Ragland D, et al. Comparative analysis of monkeypox virus infection of cynomolgus macaques by the intravenous or intrabronchial inoculation route. J Virol **2010**; 85:2112–25.
21. Sofi Ibrahim M, Kulesh DA, Saleh SS, et al. Real-time PCR assay to detect smallpox virus. J Clin Microbiol **2003**; 41:3835–9.
22. Edghill-Smith Y, Bray M, Whitehouse CA, et al. Smallpox vaccine does not protect macaques with AIDS from a lethal monkeypox virus challenge. J Infect Dis **2005**; 191:372–81.
23. Stittelaar KJ, Neyts J, Naesens L, et al. Antiviral treatment is more effective than smallpox vaccination upon lethal monkeypox virus infection. Nature **2006**; 439:745–8.
24. Earl PL, Americo JL, Wyatt LS, et al. Recombinant modified vaccinia virus Ankara provides durable protection against disease caused by an immunodeficiency virus as well as long-term immunity to an orthopoxvirus in a non-human primate. Virology **2007**; 366:84–97.
25. Chapman JL, Nichols DK, Martinez MJ, Raymond JW. Animal models of orthopoxvirus infection. Vet Pathol **2010**; 47:852–70.
26. Martin DB. The cause of death in smallpox: an examination of the pathology record. Mil Med **2002**; 167:546–51.
27. Collins J. CT signs and patterns of lung disease. Radiol Clin North Am **2001**; 39:1115–35.
28. Gattinoni L, Caironi P, Pelosi P, Goodman LR. What has computed tomography taught us about the acute respiratory distress syndrome? Am J Respir Crit Care Med **2001**; 164:1701–11.
29. Rodrigues RS, Miller PR, Bozza FA, et al. FDG-PET in patients at risk for acute respiratory distress syndrome: a preliminary report. Intensive Care Med **2008**; 34:2273–8.
30. Barton ES, White DW, Cathelyn JS, et al. Herpesvirus latency confers symbiotic protection from bacterial infection. Nature **2007**; 447: 326–9.
31. Berg RE, Crossley E, Murray S, Forman J. Memory CD8+ T cells provide innate immune protection against *Listeria monocytogenes* in the absence of cognate antigen. J Exp Med **2003**; 198:1583–93.
32. Mackaness GB. The immunological basis of acquired cellular resistance. J Exp Med **1964**; 120:105–20.
33. Mackaness GB. The influence of immunologically committed lymphoid cells on macrophage activity in vivo. J Exp Med **1969**; 129: 973–92.
34. Selin LK, Brehm MA, Naumov YN, et al. Memory of mice and men: CD8+ T-cell cross-reactivity and heterologous immunity. Immunol Rev **2006**; 211:164–81.
35. Earls JP, Cerva D Jr, Berman E, et al. Inhalational anthrax after bioterrorism exposure: spectrum of imaging findings in two surviving patients. Radiology **2002**; 222:305–12.

36. Krol CM, Uszynski M, Dillon EH, et al. Dynamic CT features of inhalational anthrax infection. AJR Am J Roentgenol **2002**; 178: 1063–6.
37. Bay A, Etlik O, Oner AF, et al. Radiological and clinical course of pneumonia in patients with avian influenza H5N1. Eur J Radiol **2007**; 61:245–50.
38. Bellani G, Guerra L, Pesenti A, Messa C. Imaging of lung inflammation during severe influenza A: H1N1. Intensive Care Med **2010**; 36:717–8.
39. Lu PX, Wang YX, Zhou BP, et al. Radiological features of lung changes caused by avian influenza subtype A H5N1 virus: report of two severe adult cases with regular follow-up. Chin Med J (Engl) **2010**; 123: 100–4.
40. Mollura DJ, Asnis DS, Crupi RS, et al. Imaging findings in a fatal case of pandemic swine-origin influenza A (H1N1). AJR Am J Roentgenol **2009**; 193:1500–3.
41. Aviram G, Bar-Shai A, Sosna J, et al. H1N1 influenza: initial chest radiographic findings in helping predict patient outcome. Radiology **2010**; 255:252–9.
42. Bleeker-Rovers CP, van der Meer JW, Oyen WJ. Fever of unknown origin. Semin Nucl Med **2009**; 39:81–7.
43. Burrill J, Williams CJ, Bain G, Conder G, Hine AL, Misra RR. Tuberculosis: a radiologic review. Radiographics **2007**; 27:1255–73.
44. Frazier AA, Franks TJ, Galvin JR. Inhalational anthrax. J Thorac Imaging **2006**; 21:252–8.
45. Ketai L, Paul NS, Wong KT. Radiology of severe acute respiratory syndrome (SARS): the emerging pathologic-radiologic correlates of an emerging disease. J Thorac Imaging **2006**; 21:276–83.
46. Lee EY, McAdam AJ, Chaudry G, Fishman MP, Zurakowski D, Boiselle PM. Swine-origin influenza a (H1N1) viral infection in children: initial chest radiographic findings. Radiology **2010**; 254:934–41.